Finite element modeling of heating phenomena of cracks excited by high-intensity ultrasonic pulses*

Chen Zhao-Jiang(陈赵江), Zheng Jiang(郑 江), Zhang Shu-Yi(张淑仪)†,
Mi Xiao-Bing(米小兵), and Zheng Kai(郑 凯)

Laboratory of Modern Acoustics, Institute of Acoustics, Nanjing University, Nanjing 210093, *China*

(Received 11 April 2010; revised manuscript received 23 May 2010)

A three-dimensional thermo-mechanical coupled finite element model is built up to simulate the phenomena of dynamical contact and frictional heating of crack faces when the plate containing the crack is excited by high-intensity ultrasonic pulses. In the finite element model, the high-power ultrasonic transducer is modeled by using a piezoelectric thermal-analogy method, and the dynamical interaction between both crack faces is modeled using a contact-impact theory. In the simulations, the frictional heating taking place at the crack faces is quantitatively calculated by using finite element thermal-structural coupling analysis, especially, the influences of acoustic chaos to plate vibration and crack heating are calculated and analysed in detail. Meanwhile, the related ultrasonic infrared images are also obtained experimentally, and the theoretical simulation results are in agreement with that of the experiments. The results show that, by using the theoretical method, a good simulation of dynamic interaction and friction heating process of the crack faces under non-chaotic or chaotic sound excitation can be obtained.

Keywords: ultrasonic infrared imaging, frictional heating of cracks, acoustic chaos, finite element method

PACC: 8170C, 4325, 4340

1. Introduction

As a novel hybrid ultrasonic/infrared nondestructive testing (NDT) technique, ultrasonic infrared (UIR) imaging, has received much more attention in recent years.[1−4] In this method, first, an intensive ultrasonic pulse generated by a high-power ultrasonic transducer is infused into a tested sample. Then, due to the interaction of the ultrasound waves (vibrations) with the defects (cracks) in the sample, the ultrasound energy transforms into heat energy. As a result, the temperature increases in the vicinity of the cracks. Next, the temperature field in the sample is imaged by an infrared camera, by which the locations and sizes of the temperature-increased areas, i.e., the cracks, can be detected. For explaining the mechanism of the localised heating, several studies were presented in recent years, such as, Mi and Zhang[5] presented a theory and finite element method (FEM) codes to calculate the ultrasonic field distribution in a plate with a crack and heating around the crack; Mian *et al.*[6] reported an FEM computation for the response of a sub-surface fatigue damage under sonic load, and Han *et al.*[7] described a finite element model to calculate the energy dissipation of a crack zone detected in UIR imaging. During the above researches, the ultrasonic excitation was modeled by a time-dependent sinusoidal displacement load at the surfaces of the sample or represented by a small cylindrical object with a prescribed sinusoidal motion. In other words, the high-power ultrasonic transducer system was completely not included in the FEM modeling, which may lead the simulation results to be not very accurate. In addition, the influence of acoustic chaos on crack heating has been analysed by using an FEM modeling of a plate, which may bounce between a cylindrical object (horn) and a rigid support post.[7] However, the FEM modeling did not consider the preload force between the horn and the sample, which are very important to the generation of acoustic chaos.[8] Moreover, in many UIR experiments, no rigid support post is included. Therefore, further studies are necessary for understanding the mechanism of heating phenomena of the cracks excited by high-intensity ultrasonic pulses.

In this paper, a three-dimensional thermo-

*Project supported by the National Natural Science Foundation of China (Grant No. 10574073).
†Corresponding author. E-mail: zhangsy@nju.edu.cn
© 2010 Chinese Physical Society and IOP Publishing Ltd

mechanical coupled FEM model is built up to simulate the phenomena of the dynamical contact and frictional heating of the crack faces when the plate containing the crack is excited by a high-intensity ultrasonic pulse. In the FEM model, the high-power ultrasonic transducer is modeled by using a piezoelectric thermal-analogy method, and the dynamical interaction between the crack faces is modeled using a contact-impact theory. The penalty method is used as a contact-impact algorithm to simulate the contact behaviour between the crack faces. Moreover, based on the first law of thermodynamics, the frictional heating taking place at both faces is quantitatively calculated by using FEM thermal-structural coupling analysis. During the FEM simulation, a hybrid combination of explicit and implicit time-integration methods is adopted, in which the central difference method (explicit) is used to calculate the elastodynamic equation, while Newmark method (implicit) is used to calculate the thermal conduction equation. Thus, the vibration behaviour and contact force characteristics of the crack faces, the time-dependent temperature distribution and temperature rise in the crack zone, as well as the influence of acoustic chaos to the crack heating, can be calculated and analysed in detail. Finally, several related experiments are also accomplished to verify the results of the theoretical simulations.

2. FEM modeling and analyses

Since transient FEM analyses can be used to simulate geometric, material and contact nonlinearity, it can be also used to solve dynamic response of structures suffering arbitrary loading. Therefore, it is very suitable to simulate the phenomenon of dynamical contact and frictional heating of crack faces by the transient FEM analyses. During the transient FEM analysis, implicit (NEWMARK type) and explicit (central difference) numerical time integration schemes are usually available to compute the transient dynamic phenomena.[9] For nonlinear problems, in each solution step of the implicit method, a NEWTON type iteration is involved. Therefore, convergence problems may occur, especially when frequent changes in the contact state exist. On the other hand, by selecting small time steps based on COURANT condition,[9] the explicit integration algorithm has good stability and fast calculation capability, which makes it suitable for simulating transient processes of short durations. Moreover, with a great variety of contact types and parameters, the explicit finite element programs, such as LS-DYNA[9] are more adept in the contact-impact (vibro-impact) simulations.[10] In our problem, the contact states between the ultrasonic horn tip and the plate surface, and also between both crack faces, change frequently, which are rather complex. Therefore, the explicit scheme is chosen and all transient computations are made with LS-DYNA.

2.1. FEM modeling of piezoelectric transducer using thermal analogy method

In the typical experimental setup of UIR imaging for crack detection, the short ultrasonic pulse is injected into the sample by a high-power ultrasonic transducer.[1,2] Owing to the complex interaction between the transducer and sample that may occur during the inspection process, the ultrasonic transducer should be modeled reasonably. FEM is widely used for the design of high-power piezoelectric actuator.[11] A lot of FEM codes allow to simulate the piezoelectric-mechanical coupling behaviour. However, FEM analysis or simulation of a complete piezoelectric actuator including contact nonlinearity stills scarce.[12] On the other hand, as described above, explicit type of FEM is prior to the simulation of the experimental phenomena including strong vibro-impact behaviour. Nevertheless, most explicit FEM codes like LS-DYNA and ABAQUS/Explicit are not possible to simulate the piezoelectric field coupling due to the absence of piezoelectric elements.[12] Thus, here, the vibration excitation of piezoelectric transducer is realised by thermal analogy method.[13]

According to the experimental conditions, a three-dimensional (3D) FEM modeling of the transducer is established, and the modal and harmonic analyses are performed by ANSYS. The simulated transducer is composed of six PZT-8 piezo-ceramic discs, a cylinder-shaped back mass (stainless steel) and a front mass (aluminium alloy), and a composite ultrasonic horn (titanium alloy). For simplicity, the bolt and pre-stress are ignored in the model. The corresponding mesh modeling is shown in Fig. 1(a).

The Block–Lanczos method[11] is chosen to calculate the natural frequency and modal shape of the transducer. During the analyses, no structural constraint is used. By modal analyses, it is found that

the resonance frequency of the longitudinal vibration mode of the transducer system is 19.99 kHz, which is very close to the oscillating frequency of the transducer used in the experiments. The harmonic analysis is then performed over a frequency range 18–22 kHz, in which sinusoidally varying input voltage of 1000 volts across the piezo-ceramic discs are used as excitation source. During the analyses, the total Rayleigh stiffness damping parameter[12] β is adopted to achieve desired vibration amplitude at the horn tip as shown in Fig. 1(b) (solid line), in which the maximum amplitude 80 μm occurs under the resonance excitation at the frequency about 20 kHz.

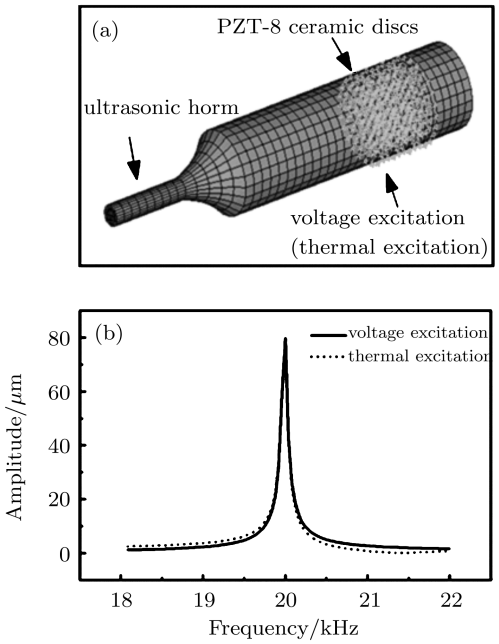


Fig. 1. FEM modeling of high-power ultrasonic transducer: (a) meshing; (b) response of transducer horn.

Then, the harmonic analyses of the transducer under thermal excitation are also performed for subsequent LS-DYNA application. According to the piezoelectric thermal analogy theory, a piezoelectric-thermal strain relationship is obtained:[13]

$$[\boldsymbol{d}]^{\mathrm{T}}\{\boldsymbol{E}\} = \{\boldsymbol{\alpha}\}\,\Delta T, \tag{1}$$

where $[\boldsymbol{d}]$ is 3×6 piezoelectric coupling matrix (strain-charge form), $\{\boldsymbol{E}\}$ is the 3×1 electric field vector; $\{\boldsymbol{\alpha}\}$ is a 6×1 thermal expansion coefficient vector, and ΔT is temperature difference between both surfaces of piezoelectric discs. If only normal electric field is applied (i.e. in one-dimensional actuation case), an exact analogy between piezoelectric strain and thermal strain is obtained through the following relation

$$d_{3i}\frac{\Delta\phi_3}{t} = \alpha_i \Delta T, \quad (i = 1, \ldots, 3), \tag{2}$$

where $\Delta\phi_3$ represents the voltage difference between both electrodes, and t is the thickness of a piezoelectric disc. Equation (2) indicates that the voltage excitation of a piezocermic disc can be simulated exactly using the conventional 3D elastic elements with the thermal actuation rather than using piezoelectric elements, but the piezoelectric elements are not currently available by LS-DYNA. One has to impose the thermal expansion coefficient α_i as d_{3i} and to impose a temperature change ΔT equal to $\Delta\phi_3/t$. Similarly, the harmonic analysis is performed and the result is also shown in Fig. 1(b) (dotted line). It can be found that the result of using thermal excitation is nearly equal to that of using voltage excitation. Therefore, it can be deduced that the piezoelectric-thermal analogy can be used for high-power ultrasonic transducer simulation.

2.2. FEM modeling of dynamical contact of cracks excited by ultrasonic pulse

A thermal-structural coupled simulation of frictional heating of micro-cracks excited by high-intensity ultrasonic pulses is performed subsequently in LS-DYNA when the reasonable response of the ultrasonic transducer is obtained. The FEM modeling includes two parts: a plate containing a crack is used as a sample, and an ultrasonic transducer described above is used to excite the sample. Moreover, for modeling the static coupling (preload) force F_{s} in the experiments, an alterable acceleration loading G_{s} is applied to the whole transducer system.

The plate is of a size of 120 mm×60 mm×2.5 mm and has a notch about 8 mm×2 mm×2.5 mm at the top side. A through-thickness crack with V-shape is located just below the notch. The crack is of a length about 3 mm and the width of the upper open ending is about 5 μm and then gradually reduced to be closed. The structural and thermal properties of 2024-T351 aluminum alloy plate listed in Table 1 are for the sample. The finite element mesh and geometry of the model is shown in Fig. 2(a). The plate is meshed with 8-node hexahedral elements and three layers in the thickness. For describing accurately the contact interaction between both crack faces and giving a precise description of the heat generation and spread in

the crack region, artificial meshing is chosen instead of automatic meshing to vary the mesh density in the model, which allows a fine mesh at the crack interface. Figure 2(b) represents the finite element mesh in the vicinity of the crack, where it can be found that the number of divisions on the crack length is 15. The total number of the elements in the plate is about 9230. The applied boundary conditions of the plate are that all degrees of freedom of the displacements are constrained at the nodes of the left and right sides of the plate, but are free along the two other parallel sides (upper and lower sides) of the plate. The initial temperature of the plate sample is assumed to be 27.0 °C.

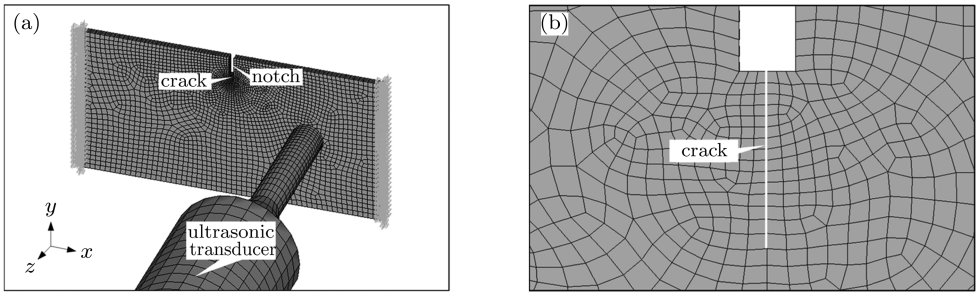


Fig. 2. FEM modeling of plate containing a crack excited by high-power ultrasonic transducer: (a) global finite element mesh; (b) enlarged finite element mesh in the vicinity of the crack.

Table 1. Physical parameters of aluminum 2024-T351.

heat conductivity/(W/m · K)	specific heat/(J/kg · K)	density/(kg · m^{-3})	Young's modulus/GPa	Poisson's coefficient
121	875	2780	73.1	0.33

The contact interaction between the ultrasonic horn tip and the plate surface, and the contact interaction between both crack faces are very important to the plate vibration behaviour and subsequent crack heating. During the simulation, the interface between the horn tip and the plate is assumed to be unbonded. According to LS-DYNA,[14] here, the surface of the horn tip is designated as the master side and the plate surface around the contact region is designated as slave side. For the crack faces contact modeling, one side of the crack is declared as a master surface and the other one is a slave surface. The nodes lying in those surfaces are referred to as the slave and master nodes, respectively. In current model, penalty method is used in formulating the contact mechanisms, and 'surface-to-surface' contact algorithm is chosen.[14] If the interface pressure becomes large, unacceptable penetration may occur. However, the overall deformation in the present simulation is very small and is of the order of a few microns. So, unacceptable penetration may not occur at the interface, and hence scaling down of the time step size will not be required. However, during the simulation, smaller time step size is needed owing to the refined mesh in the contact region. For reducing computation costs, the mass-scaling technique[14] is applied in the simulations, and the computation efficiency is improved obviously.

2.3. Frictional heating of cracks

In this work, an important coupling between thermal and mechanical energies has been achieved through the heat generation caused by the friction when the crack faces slide relative to each other. Specifically, assuming that the slave node $n_{\rm s}$ is in contact with the master segment (segments) at time t and $t+\Delta t$, and the displacement increment is Δe, thus the equivalent heat flux q of frictional heating can be written as

$$q = \varsigma \cdot \tau \cdot v, \tag{3}$$

where ς is the coefficient of frictional dissipation energy converted into heat, τ is the friction stress, and $v = \Delta e/\Delta t$ is the slip velocity of the slave node $n_{\rm s}$ relative to the master segment.

Assuming that the heat generation due to friction is equally distributed over both contact surfaces,

and the slave node and the master segment are both receiving half of the heat flux q. Similarly, through the shape function N,[15] the heat flux on the master segment is further distributed over the nodes of the master segment.

Next, the 3D transient thermal conduction equation can be written as[14]

$$\boldsymbol{L}\dot{\boldsymbol{\Phi}} + \boldsymbol{H}\boldsymbol{\Phi} = \boldsymbol{Q}, \tag{4}$$

where $\boldsymbol{Q} = \sum \int_{\mathrm{V}} qN \,\mathrm{d}V$, $\boldsymbol{\Phi}$ is the node temperature array, $\dot{\boldsymbol{\Phi}} = \mathrm{d}\Phi/\mathrm{d}t$ is the array of temperature variation rate; and $\boldsymbol{L}$, $\boldsymbol{H}$ and $\boldsymbol{Q}$ are the heat-capacity, heat-conduction, and heat-loading matrices, respectively. The Coulomb model[16] is employed to simulate the friction process, and the friction coefficient is assumed to be 0.4 between the crack faces. The Crank–Nicolson method[14] is used as an implicit integral method to solve thermal conduction equation (4). By solving Eq. (4), the transient temperature field can be obtained. On one hand, the temperature in the vicinity of the crack is generally not high, and on the other hand, the behaviour we are concerned with lasts only a few milliseconds. Thus, the heat convection and radiation can be ignored.

3. Numerical results and discussions

Obviously, there are many factors affecting the UIR signals, such as the location and amplitude of the ultrasonic source. However, when a sonic source in low frequency range (15 to 40 kHz) is used, the location of the sonic source is not critical.[17] On the other hand, the presence or absence of the nonlinearity of the coupling between the test specimen and the acoustic horn makes a significant difference in the detectability of cracks.[3] It has been observed in the experiments that, although the ultrasonic excitation source is highly tuned, the vibrations in the object under testing by UIR may be quite complicated, even acoustic chaos may appear.[18,19] Since the plate vibration characteristics under sound non-chaotic and chaotic excitations have important influences to the motions of crack-faces, the FEM simulations of frictional heating phenomena of cracks are discussed separately according to different conditions.

3.1. Crack heating when undergoing sound non-chaotic excitation

It has been observed in the simulation that the vibration amplitude of the horn and the preload force of the transducer system are very important to the vibration condition of the plate. It seems that a particular combination of vibration amplitude and preload force is crucial to generate the sound chaotic excitation. If the preload force is great enough, the corresponding indentation depth may be larger than the vibration amplitude, leading to that the tip of the horn will not recoil from the surface during the negative half of the acoustic period. As a result, no subharmonic (or quasi-subharmonic) frequencies[8] will occur in the plate vibration spectrum and the plate can be considered as undergoing sound non-chaotic excitation.

Figure 3 displays the calculated result of non-chaotic vibration waveform and the corresponding frequency spectrum of the out-of-plane motion (Z-direction) of a node of the plate, where the node is located at the centre of the contact region between the plate and the horn tip; the preload force of the transducer system is 525 N. As shown in Fig. 3(a), the plate vibration spectrum consists mainly of the 20 kHz excitation frequency component, though many harmonics are present. The expanded display of the velocity waveform in Fig. 3(a) is shown in Fig. 3(b), where the waveform is nearly a sinusoidal function with single frequency. Corresponding to the velocity waveform in Fig. 3(a), the time history and Fourier spectrum of the contact force between the horn and the plate are shown in Fig. 3(c). It also can be found that many harmonics of 20 kHz frequency are present, indicating that the superharmonic vibration of the plate is induced by the contact force containing superharmonic components. An expanded region of the contact force waveform of 80.0–80.5 ms is displayed in Fig. 3(d), in which the obvious period corresponding to the primary excitation frequency (20 kHz) can be clearly observed. As a result, the plate vibration condition in Fig. 3 can be considered as non-chaotic.

It should be mentioned that the complex vibration of the plate leads the contact pressure pattern across the crack faces to becoming complicated both spatially and temporally. According to the vibration condition in Fig. 3 (non-chaotic case), the resultant interface force waveform (contact pressure) for the crack faces and the corresponding force spectrum are shown in Fig. 4(a). Compared with the amplitude of the

contact force between the horn and the plate, the amplitude of the contact force between the crack faces is very small, about a dozen of Newton (inset). It can be seen that the force spectrum also consists principally of 20 kHz and its harmonics. However, owing to the contact interaction (contact nonlinearity) of both crack faces,[20,21] the amplitude ratio between the harmonics and the fundamental component becomes larger compared with that in Fig. 3(b). For observing clearly the waveform of the contact force, Fig. 4(b) displays the time history of nodal interface force of a mesh node on the crack face in an expanded time scale, where the distance between the node and the crack tip is about 0.8 mm. It can be found that the contact force waveform of the crack faces is composed of a series of force pulses that have nearly equal magnitudes. Moreover, it is observed that different nodes on the crack faces may have different magnitudes of the contact forces.

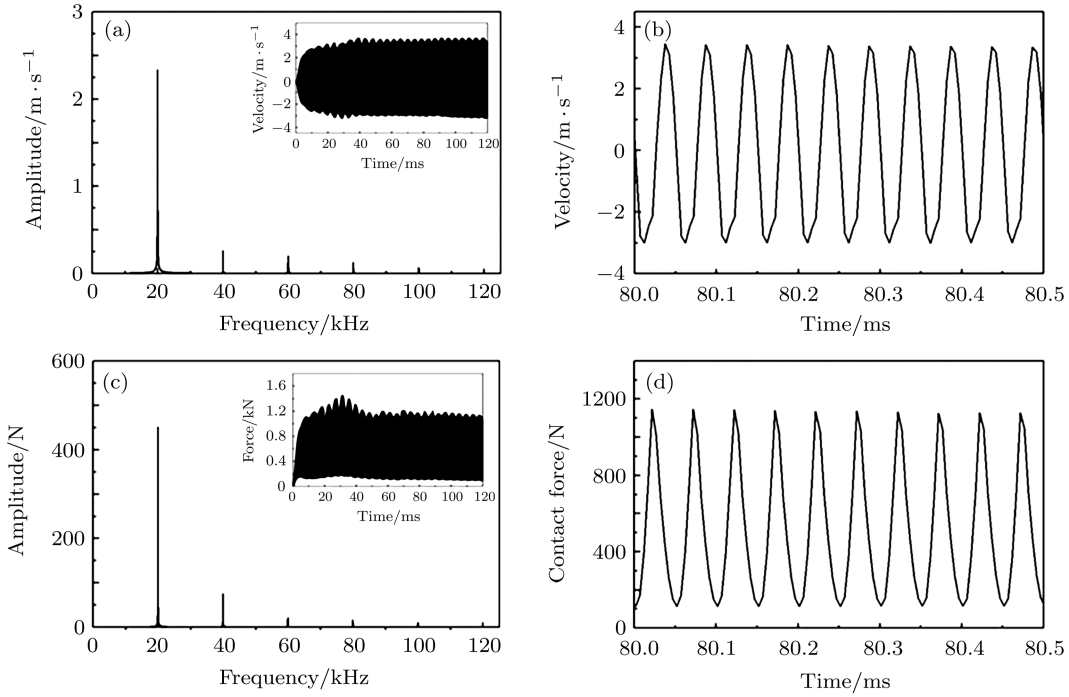


Fig. 3. Calculated results of non-chaotic vibration of the plate excited at 20 kHz: (a) vibration waveform (inset) and frequency spectrum; (b) expanded section (80.0–80.5 ms) from (a); (c) contact force waveform (inset) and Fourier spectrum; (d) expanded section (80.0–80.5 ms) from (c).

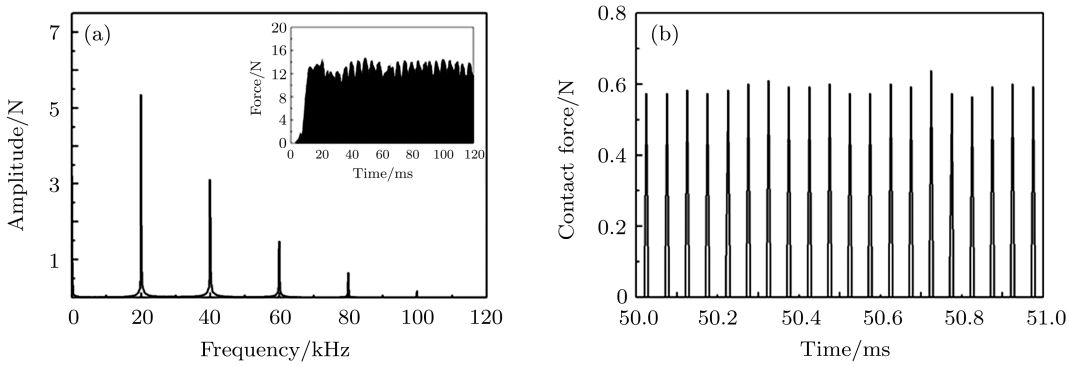


Fig. 4. Calculated results of contact force between the faces of crack under non-chaotic condition: (a) force waveform (inset) and spectrum; (b): expanded section (50.0–51.0 ms) of contact force waveform of a node located on crack face and 0.8 mm from the crack tip.

To produce frictional heating, it is important to find out the differential motions of both crack faces. A numerical result of the differential out-of-plane velocity of two nodes on the crack undergoing sound non-chaotic

excitation is shown in Fig. 5, where both nodes are located separately at the left and right faces of the crack but at the same distance (about 0.4 mm) from the crack tip. It can be found in the inset of Fig. 5(a) that there exists differential motion between the two crack faces. Moreover, it is also found that different nodes on the crack faces have different amplitudes of differential velocity. The amplitude of the differential velocity waveform of the upper portion of the crack is much bigger than for the bottom portion of the crack. From the expanded waveform in Fig. 5(b), it can be observed that the velocity waveform still varies in periodicity. It can be found in Fig. 5(a) that the velocity spectrum includes many superharmonics, and the amplitude of 2nd harmonics is almost the same as that of the fundamental.

From the above numerical results it can be found that frictional heating phenomena may occur at the crack faces as the ultrasonic excitation pulse is incident on. The temperature distributions around the crack area undergoing sound non-chaotic excitation are shown in Fig. 6, where the middle region of the crack appears the hottest. In Fig. 7, the temperature increment vs time curves are shown for two different nodes on the left crack face. One is near the crack tip and the other one is in the middle region of the crack. It can be observed that the temperature rises quickly when the ultrasonic excitation being. However, owing to heat diffusion around the crack region, temperature cannot always rise during the ultrasonic excitation process. It is clearly seen that the temperature increment is higher in the middle region than at the crack tip, which is the same as shown in Fig. 6. The reason is that the crack middle portion has larger differential displacement between both crack faces and more thermal energies are generated. Moreover, the temperature rise-time curve is relatively smooth when the plate is undergoing sound non-chaotic excitation. However, the generated heat energy under non-chaotic excitation is small, which makes the crack detection to be difficult.

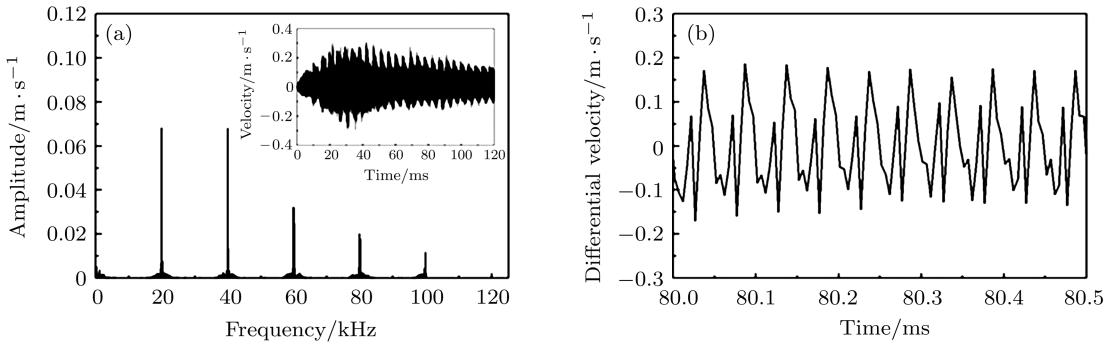


Fig. 5. Calculated results of differential out-of-plane velocity of two nodes located at the right and left faces of crack separately and 0.4 mm from crack tip under non-chaotic condition: (a) velocity waveform (inset) and frequency spectrum; (b) expanded section of velocity (80.0–80.5 ms) from (a).

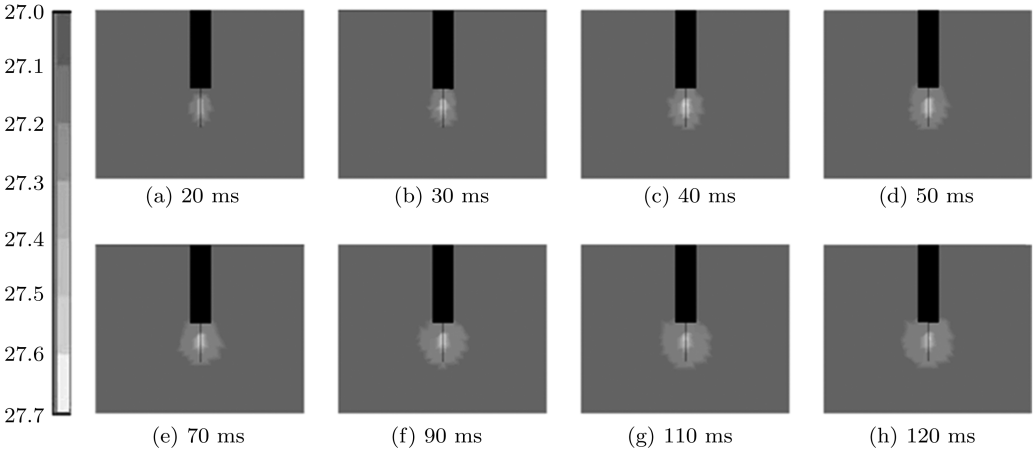


Fig. 6. Calculated results of temperature distributions around crack under non-chaotic condition.

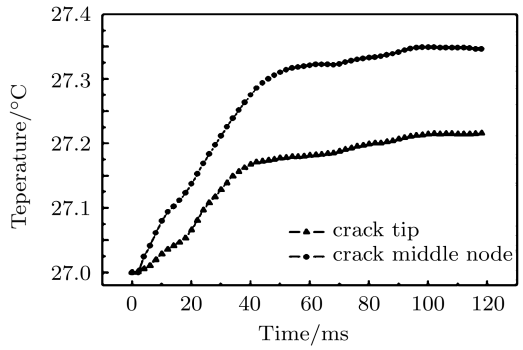


Fig. 7. Calculated results of temperature-time curves for two nodes located separately at both crack faces under non-chaotic condition.

3.2. Crack heating under sound chaotic condition

When the preload force of the transducer is suitable, in addition to harmonic components, the plate vibration spectrum also contains many subharmonic and ultra-subharmonic components, which means that the plate is undergoing strong sound chaotic excitation. Figure 8 shows the calculated results of the plate vibration when the preload force is equal to 150 N, a chaotic vibration being shown in Fig. 8(a). It is obvious that the amplitude of the chaotic vibration waveform in Fig. 8(a) is larger than that of the non-chaotic vibration waveform in Fig. 3(a). Moreover, it can be observed that the chaotic waveform is more complex as shown in the expanded waveform in Fig. 8(b). The time history obtained from Fig. 8(a) and the corresponding Fourier spectrum of the contact force between the horn tip and plate surface are shown in Fig. 8(c). It can be found that many subharmonic components are present and the order number of the subharmonics is the same as the plate vibration spectrum (order 13). Comparing with Fig. 3(c), it can be found that the contact force under sound chaotic excitation has larger amplitude as shown in Fig. 8(c). It also can be found that the contact force waveforms under sound non-chaotic and chaotic conditions have clearly different characteristics. In Fig. 8(d), the expanded contact force waveform consists of a series of separated force pulses and different force pulses may have different amplitudes rather than the continuous waveform in Fig. 3(d).

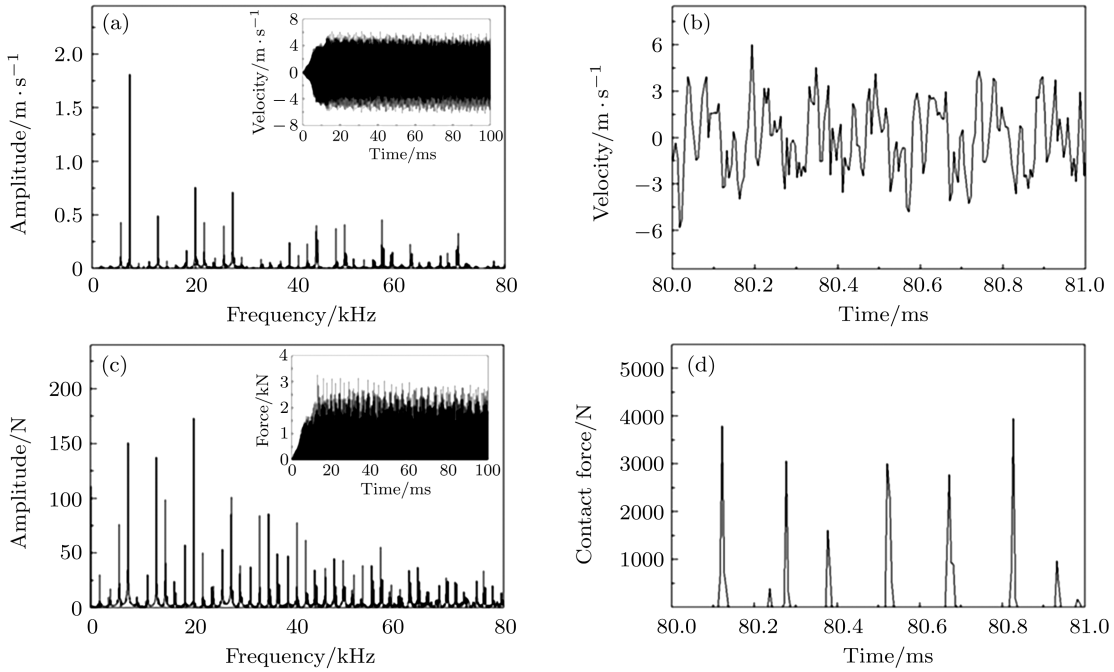


Fig. 8. Calculated results of chaotic vibration of plate excited at 20 kHz: (a) vibration waveform (inset) and frequency spectrum; (b) expanded section (80.0–80.5 ms) from (a); (c) contact force waveform (inset) and Fourier spectrum; (d) expanded section (80.0–80.5 ms) from (c).

According to the condition of sound chaotic condition in Fig. 8, the resultant contact force (inset) between the crack faces and the corresponding Fourier spectrum is shown in Fig. 9(a). Compared with Fig. 4(a), the amplitude of the contact force in Fig. 9(a) is larger. Moreover, the Fourier spectrum of waveform in Fig. 9(a) contains much more frequency components such as many subharmonic and ultra-subharmonic components.

Figure 9(b) displays the contact force waveform of a node on the crack face in an expanded time scale, where the distance between the node and the crack tip is about 0.8 mm. It also can be found that the contact force waveform of the crack in Fig. 9(b) also consists of a series of force pulses which have different magnitudes. Moreover, the time intervals of the adjacent force pulses may be different when the plate is undergoing sound chaotic excitation. It can be found in Fig. 9, that, though the amplitude of crack contact force is relatively large, the number of pulses in the same time interval is decreased. Therefore, the overall effect of contact pressure on frictional heating does not increase much.

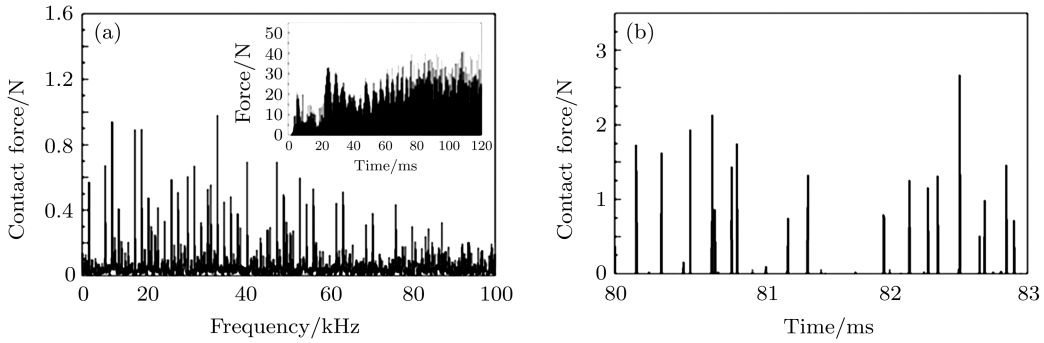


Fig. 9. Calculated results of contact force at crack faces under chaotic condition: (a) force waveform (inset) and Fourier spectrum; (b) expanded section (50.0–51.0 ms) of contact force waveform of a node located at crack face and 0.8 mm from crack tip.

Shown in Fig. 10 is a numerical result of out-of-plane differential velocity of two nodes separately located at the right and left faces of the crack and 0.4 mm from the crack tip when undergoing sound chaotic excitation. It can be found that there also exists differential motion between the two crack faces under chaotic excitation. The expanded waveform in Fig. 10(b) displays that the periodicity of the differential velocity waveform under sound chaotic excitation is not clear, and the amplitude of differential velocity under sound chaotic excitation is larger than that in Fig. 5 under sound non-chaotic excitation. The frequency spectrum of vibration waveform in Fig. 10(a) contains many subharmonic and ultra-subharmonic components, which is different from the frequency spectrum under sound non-chaotic excitation.

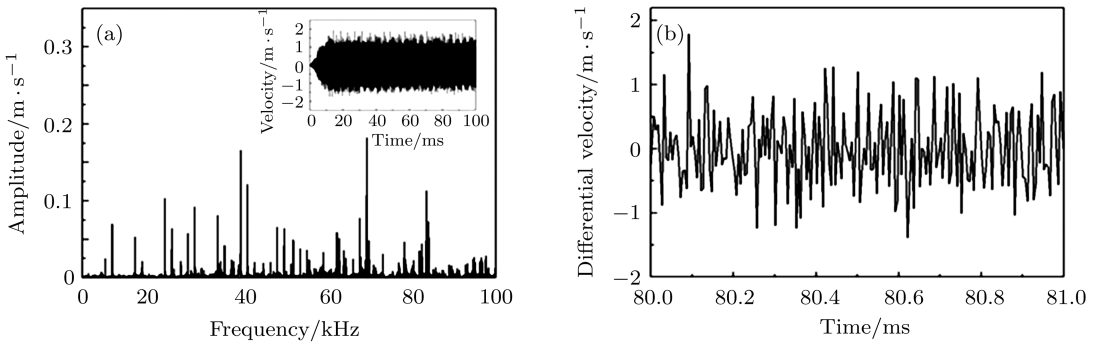


Fig. 10. Calculated results of differential out-of-plane velocity of two nodes located at right and left faces of the crack and 0.4 mm from crack tip under chaotic: (a) velocity waveform (inset) and frequency spectrum; (b) expanded section (80.0–80.5 ms) from (a).

The temperature distributions around the crack area under sound chaotic excitation are shown in Fig. 11. In order to compare clearly the heating rate of a crack under non-chaotic excitation with that under chaotic excitation, the temperature scale in the range of 27.0 °C – 27.7 °C is also used. The brightness of the crack area in Fig. 11 is obviously stronger than that in Fig. 6, which clearly indicates that the sound chaotic excitation produces a much larger temperature rise in the crack region, making the crack detection become easier. The main reason why it can be obtain a getting higher heat generation rate during the application of chaotic pulse is the presence of many higher frequency components in the chaotic pulses. These higher frequency components

help to achieve a higher differential velocity as well as higher contact forces between the crack faces than that is possible by the single excitation frequency as explained before.

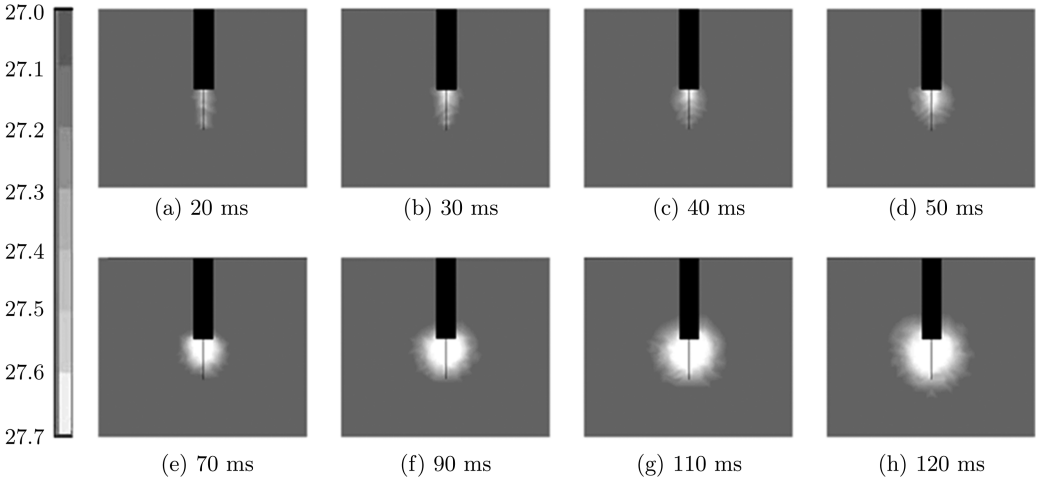


Fig. 11. Calculated results of temperature distributions around crack under chaotic condition.

The temperature versus time curves for two nodes located on the crack faces are displayed in Fig. 12, where the position of crack nodes is identical to that in Fig. 7. It is similar that the temperature increment is higher in the crack middle region than at the crack tip. By comparing Figs. 7 and 12, it can be clearly observed that the temperature rise curve under non-chaotic excitation may approach stable case (saturation) at an earlier time. When the vibration is in chaotic state, more power is available at the crack, and as a result the thermal signal is greatly enhanced, which is beneficial for the crack detection. In addition, the temperature-rise curves in Fig. 12 show that the temperature increases un-monotonously and has some fluctuation under chaotic excitation, which is induced by the intermittent contact and complex differential motion of the crack faces.

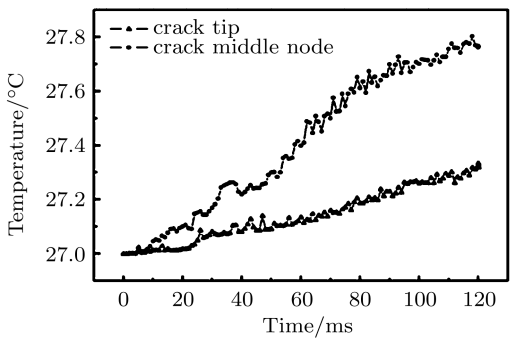


Fig. 12. Calculated results of temperature-time curves for two nodes located separately at both crack faces under chaotic condition.

4. Experimental verification

To verify the finite element computational results presented above, the surface vibration and the crack heating for an aluminum alloy plate with an edge notch and crack similar to the model above are measured experimentally by the UIR thermography system.[2] The plate is excited under both non-chaotic and chaotic acoustic conditions (320 ms duration) via a high-power ultrasonic transducer but other conditions are the same. The out-of-plane vibration of the plate is measured using a laser vibrometer.

Figure 13 shows two different vibration waveforms (insets) and frequency spectra of the plate simulated in different experiments, which are obtained with and without a thin rubber used as coupling material between the horn tip and the plate, as shown in Figs. 13(a) and 13(b), respectively. It can be found that in Fig. 13(a), only the fundamental and superharmonics occur, i.e., it is non-chaotic condition. However, in Fig. 13(b) a lot of components including fundamental, superharmonics, subharmonics and ultra-subharmonics, etc., appear, which shows the vibration is chaotic. It can be found also that the vibration amplitude of the plate under sound chaotic condition is much larger than that under non-chaotic condition, but the amplitude of the fundamental under non-chaotic case is larger than that under chaotic case. The experimental results in Fig. 13 are in agreement with the FEM simulation results in Figs. 3 and 8.

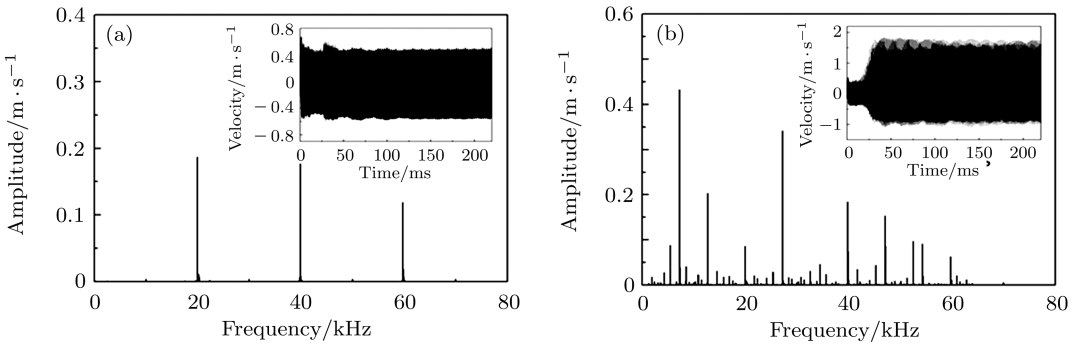


Fig. 13. Experimental results of vibration waveforms (insets) and frequency spectrums for plate under: (a) non-chaotic, and (b) chaotic excitation.

Figures 14 and 15 give the temperature distributions around the crack area undergoing the sound non-chaotic and non-chaotic excitation respectively, which illustrate the differences of generation of heat energy at the crack. It can be seen in Fig. 15 that obvious temperature rise occurs in the crack region when the plate is under sound chaotic condition. When the ultrasonic pulse is turned off at time 320 ms, the values of temperature rise in the crack region are of 0.1 °C–0.3 °C and 0.3 °C–0.8 °C are for non-chaotic and chaotic excitation respectively. Obviously, the crack detection under chaotic excitation is much sensitive than that of non-chaotic excitation. The experimental result is in agreement with the FEM simulation results.

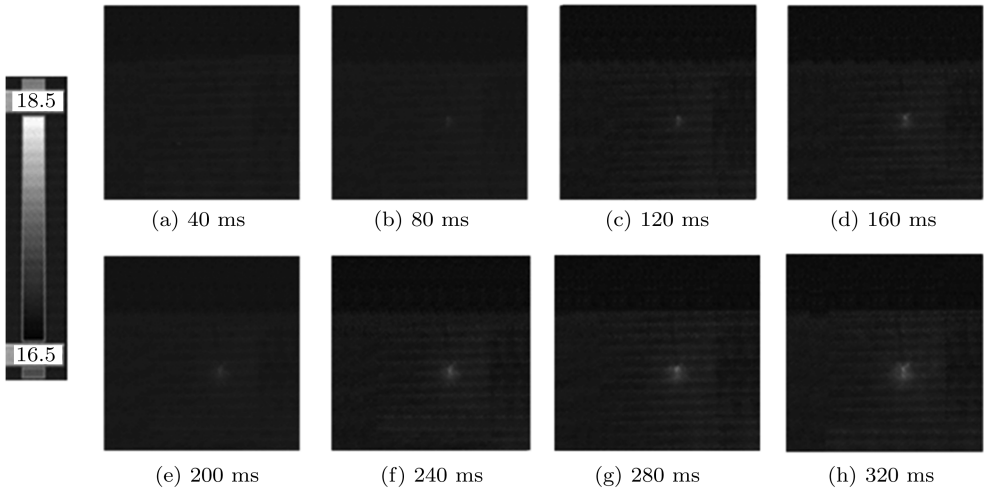


Fig. 14. Experimental results of temperature distributions around crack under non-chaotic condition.

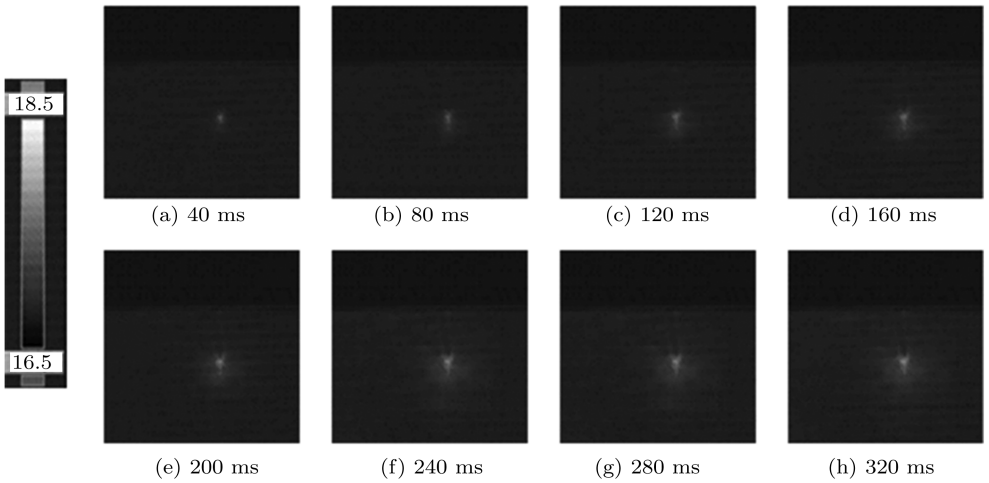


Fig. 15. Experimental results of temperature distributions around crack under chaotic condition.

Figure 16 displays the temperature-time curves for a point located at the middle of the crack of the plate under sound non-chaotic and chaotic excitations. The amplitude of temperature rise under chaotic excitation is always 2 to 3 times higher than that under non-chaotic condition. Moreover, Fig. 16 shows that the temperature rises with time rapidly at the beginning, then gradually approaches saturation owing to the diffusion of heat energy. The results are also consistent with the FEM simulation above.

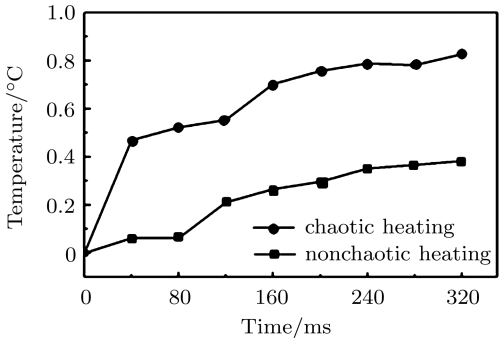


Fig. 16. Experimental results of temperature-time curves of a point located at the middle of crack under chaotic and non-chaotic conditions.

5. Conclusions

The mechanism of the crack detection based on frictional heating by using UIR imaging has been further studied by using finite element modeling. Several typical conclusions can be obtained as follows.

(i) In the dynamic interaction process of crack under ultrasonic excitation, both crack faces will produce relative motion, then contacting, slipping and separating will occur on the crack faces. As a result, the frictional heating is produced in the crack area.

(ii) In the process of ultrasonic excitation, the amplitudes and phases of the motions of both crack faces are different. Chaotic sound excitation causes a greater differential motion across the crack, which probably results from the abundant frequency components present in the plate.

(iii) The time dependence of the pressure (force) pattern across the crack faces is complicated spatially and temporally. The waveform of the contact force consists of a series of delta pulses. For the non-chaotic excitation, all of the force pulses have nearly the same magnitudes and time intervals, and the Fourier spectrum is dominated by the excitation frequency and harmonics. For the chaotic condition, the magnitudes and time intervals of the force pulses are different, and there may contain many subharmonic and ultra-subharmonic components, etc., in the corresponding Fourier spectrum.

(iv) From the simulated and experimental results, it is observed that acoustic chaos can produce much more heating energy than the non-chaotic condition.

(v) The temperature-rise curves under sound non-chaotic and chaotic conditions have some obvious differences, e.g. the temperature-rise curves under non-chaotic condition are monotonous and smooth, however, there exist some fluctuations under chaotic condition, which just indicate that intermittent contact occurs at the crack faces.

(vi) To verify the theoretical results, several related experiments have been carried out, which show that the experimental results are consistent with those of theoretical simulations. Therefore the theoretical results can be used to quantitatively explain the phenomena observed in UIR imaging and are helpful for understanding and extending the applications of this technique.

References

[1] Favro L V, Han X Y, Ouyang Z, Sun G, Sui H and Thomas R L 2000 *Rev. Sci. Instrum.* **71** 2418
[2] Hong Y, Miao P C, Zhang Z N, Zhang S Y and Shui X J 2004 *Acoust. Sci. Technol.* **25** 77
[3] Han X Y, Zeng Z, Li W, Islam M S, Lu J P, Loggins V, Yitamben E, Favro L D, Newaz G and Thomas R L 2004 *J. Appl. Phys.* **95** 3792
[4] Morbidini M and Cawley P 2009 *J. Appl. Phys.* **105** 093530
[5] Mi X B and Zhang S Y 2004 *Prog. Nat. Sci.* **14** 628 (in Chinese)
[6] Mian A, Newaz G, Han X Y, Mahmood T and Saha C 2004 *Compos. Sci. Technol.* **64** 1115
[7] Han X Y, Islam M, Newaz G, Favro L V and Thomas R L 2006 *J. Appl. Phys.* **99** 074905
[8] Chen Z J, Zhang S Y and Zheng K 2010 *Acta Phys. Sin.* **59** 4071 (in Chinese)
[9] Ingolf M, Alexander K, Peter V and Karl S 2005 *Eng. Struct.* **27** 191
[10] Wang L, Xu W and Li Y 2008 *Chin. Phys.* B **17** 2446
[11] Abdullah A and Pak A 2008 *Int. J. Adv. Manufact. Techn.* **39** 21
[12] Potthast C, Twiefel J and Wallaschek J 2007 *J. Sound Vib.* **308** 405
[13] Cote F, Masson P, Mrad N and Cotoni V 2004 *Compos. Struct.* **65** 471
[14] Hallquist J O 2006 *LS-DYNA Theory Manual* (Livermore: LSTC)

[15] Cook R D, Maklus D S, Plesha M E and Witt R J 2001 *Concepts and Applications of Finite Element Analysis* (New York: Wiley)

[16] Mabrouki F, Thomasb M, Genesta M and Fahr A 2009 *NDT & E Int.* **42** 345

[17] Han X, Favro L D, Ouyang Z, Thomas R L 2002 *AIP Conf. Proc.* **615** 552

[18] Han X Y, Li W, Zeng Z, Favro L D and Thomas R L 2002 *Appl. Phys. Lett.* **81** 3188

[19] Chen Z J, Zhang S Y, Zheng K and Kuo P K 2009 *J. Appl. Phys.* **106** 023507

[20] Okada J, Ito T, Kawashima K and Nishimura N 2001 *Jap. J. Appl. Phys.* **40** 3579

[21] Zhou D, Liu X Z, Gong X F, Nazarov V E and Ma L 2009 *Chin. Phys.* B **18** 1898